Convergent-divergent design of fins for improving the thermo-hydraulic performance of heat exchangers assisted by a dual-flow topology generator

Ahmad Fawaz, Yuchao Hua, Steven Le Corre, Yilin Fan, Lingai Luo

Convergent-divergent design of fins for improving the thermo-hydraulic performance of heat exchangers assisted by a dual-flow topology generator

Ahmad Fawaz, Yuchao Hua*, Steven Le Corre, Yilin Fan, Lingai Luo†,

Nantes Université, CNRS, Laboratoire de thermique et énergie de Nantes, LTeN, UMR6607, F-44000 Nantes, France

*Corresponding author: Email: yuchao.hua@univ-nantes.fr

†Corresponding author: Email: lingai.luo@univ-nantes.fr

Abstract

In this work, a density-based topology generator (TG) is used to maximize the effectiveness of a 2D periodic unit within the counter-flow Plate heat exchanger (PHE), resulting in a novel convergent–divergent fin arrangement. Due to the high sensitivity of the TG setting parameters, an investigation is conducted to study their effects on the acquired topologies. It is observed that the convergent-divergent distribution feature remains consistent regardless of the input parameter settings with a conspicuous variation of the acquired fins distribution. To assess the efficacy of this newly-proposed design guideline of fins, a simplified HX (heat exchanger) with convergent-divergent (C-D) rectangular fin distribution is introduced and compared with the TG-acquired structures and a conventional uniform fin design. The comparative analysis is performed by conducting a set of computational fluid dynamic (CFD) simulations on the five structures (three TG-obtained, one simplified and one conventional) under two different cases (case1: water-water, case2: water-oil as cold and hot working fluids respectively) that encompass a wide range of Reynolds numbers (300-3000). The results show a thermo-hydraulic improvement of the TG-acquired and simplified HXs compared to the conventional one with an enhancement in the performance evaluation criteria (PEC) number up to about 23% and 10% for case 1 and up to 36% and 16% for case 2, respectively. Eventually, a detailed physical interpretation of the generated topology is delivered. The current work provides a novel guideline for fin design inspired by topological features, which could be helpful to improve the performance of HXs.

Keywords: Topology generator, Heat exchanger, Convergent-divergent, Conjugate heat transfer, thermo-hydraulic performance.

Nomenclature

$f(\gamma)$	*Brinkman Coefficient*
L	*Channel width (m)*
$T_{in,cold}$	*Cold fluid inlet temperature (K)*
φ	*Constraint*
γ	*Densities (Design Variables)*
P^*	*Dimensionless pressure*
T^*	*Dimensionless temperature*
v^*	*velocity*
α^*	*Dimensionless Inverse permeability*
R	*Filter radius (m)*
γ_f	*Filtered Design Variables*
v_{in}	*Flow inlet velocity (m/s)*
ρ	*Fluid density (kg/m^3)*
k_f	*Fluid thermal conductivity (W/m.K)*
μ	*Fluid viscosity (Pa.s)*
f	*Friction coefficient*
A	*Heat transfer area (m^2)*
h	*Heat transfer Coefficient (W/m^2.K)*
Q	*Heat transfer rate (W)*
$T_{out,hot}$	*Hot fluid outlet temperature (K)*
D_h	*Hydraulic diameter (m)*
γ_i	*Initial design variable*
L	*Lagrange function*
λ	*Lagrange multipliers (adjoint variables)*
l	*Length of heat exchanger*
$LMTD$	*Logarithmic mean temperature difference (K)*
$\left\|\overrightarrow{\nabla T}\right\|$	*Magnitude of* $\overrightarrow{\nabla T}$
$\|\vec{v}\|$	*Magnitude of* $\vec{v}$
α_{max}	*Maximum inverse permeability*
$\dot{m}$	*Mass flow rate (kg/s)*
$\vec{n}$	*Normal vector*
Nu	*Nusselt Number*
q	*Penalization coefficient*
p	*Penalty factor*
Pr_f	*Prandtl Number*
ΔP	*Pressure drop (Pa)*
P	*Pressure (Pa)*
γ_p	*Projected Design Variables*
γ_β	*Projection point*
β	*Projection slope*
Er	*Relative error*
Re	*Reynolds Number*
Re_{hot}	*Re of hot fluid*
Re_{cold}	*Re of cold fluid*
v_{fs}	*Solid fraction*
k_s	*Solid thermal conductivity (W/m.K)*
C_{pf}	*Specific heat of the fluid (J/Kg.K)*
$cos\theta$	*Synergy field*
T	*Temperature (K)*
$\overrightarrow{\nabla T}$	*Temperature gradient vector*
C_k	*Thermal conductivity ratio*
γ_{th}	*Threshold value*
v	*Velocity (m/s)*
$\vec{v}$	*Velocity vector*

Abbreviations

C-D	*Convergent-divergent*
CFD	*Computational fluid dynamics*
FEA	*Finite element analysis*
FEM	*Finite element method*
GCMMA	*Globally convergent MMA*
GE	*Governing equations*
HX	*Heat exchanger*
MMA	*Method of moving asymptotes*
PHE	*Plate heat exchanger*
PEC	*Performance evaluation criteria*
TG	*Topology generator*

1. Introduction

Heat exchangers (HXs) are dispersed in almost all industrial sectors, including power plants, electronic devices, and material fabrication processes, etc. [1]–[7], which can significantly influence overall efficiency of energy systems [8]. How to improve the performance of HXs has been for a long time an essential topic in both industrial and academic communities. Over the past decades, tremendous active and passive methods have been developed for improving the effectiveness of HXs [9]. It has been well demonstrated that the utilization of extended surfaces as fins are the most effective ones in practice to enhance heat transfer rates by disrupting fluid flows and increasing surface areas, with the drawback of increasing the hydraulic loss [10], [11].

The proper design of extended surface i.e. fins, including shape, size, and arrangement, is of importance for achieving a good trade-off between heat transfer rate enhancement and pumping power requirement, especially for compact HXs like plate heat exchangers (PHE) [12],[13]. At the beginning stage, researchers generally designed fins intuitively based on their physical background and understandings [14]–[16]. Afterwards, with the development of computer techs, optimal designs of fins become possible with the assistance of numerical simulation and various optimization algorithms. Size/shape optimization of fins, which cannot significantly alter the prescribed configuration or arrangement set by designers, has been developed for years [17]–[20]. Most recently, topology optimization (TO), which acts on the topology of geometry by spatially optimizing the distribution of fluid and solid phases and thus theoretically holds maximum degrees of freedom in optimization, has attracted increasing attention from researchers [21]–[23]. The application of the TO to address conjugate heat transfer problems is associated with several limitations [23]. However, it is noteworthy that, notwithstanding these constraints, a guaranteed improvement in performance remains achievable.

Various complex and high-performance thermal designs have been obtained using TO. As for HXs, researches start with single flow TO assuming that the design domain is subjected to heat source or heat flux [24]–[26]. For instance, Kobayashi et al. [25] designed a novel winglet by applying the TO on a single flow fin-and-tube HX for heat transfer intensification purposes. Then, it was extended to dual flow HXs that exchange heat between two fluids separated by one solid [27]–[30]. As an example, Høghøj et al. [30] conducted the density-based TO on a 2D and 3D bi-flow HXs to magnify the heat

transfer rate between hot and cold fluids under a pressure drop constraint. Recently, the TO has been employed to design fin geometries to enhance the thermo-hydraulic performance for a practical HX application [31]. Even with the high ability of the additive manufacturing techniques to design complex structures, the fabricated design could have lower performance compared to the TO-derived numerical design by the reason of some limitations in the 3D printing techniques [31].

The acquired topological configurations by the TO are conspicuously affected by the choice of input parameters justifying the notable sensitivity of these input parameters on the generated topology. Currently, the TO is mainly conducted on one-flow HXs (more than 90%), according to the statistics in our recent review paper [23] that covers most of the relevant publications in the past two decades, while the HXs in practice frequently work with at least two flows. Moreover, the majority of design problems generally introduce the wide (Length/width < 2) design domains that allows the structures to evolve freely to generate highly complex structures [27]–[29], but this may contradict with some actual applications where the fluid area is considerably restricted as in compact HXs. In addition, in-depth physical interpretation on the generated structures is always needed for better understanding and possible generalization of the results. It should be noted that for the majority of conjugate heat transfer TO research [23], [32], modifications of the governing equations (as the inclusion of the artificial body force term in the density-based scheme) and filters imposition are usually required in order to guarantee the stability and efficiency of the optimization. However, those modifications can distort the exact conjugate heat transfer physics during the optimization process [32], emphasizing the necessity of high-fidelity CFD simulations along with physical analysis. In this sense, we here use the term TG (topology generator) to denote the optimization process that derives the novel designs, underscoring its basic function (topology generation) and the potential for physical distortion of heat transfer phenomena.

Considering the issues above, the present work employs the dual-flow density-based TG (subsection of TO) to handle the heat transfer within the narrow 2D design domain (of large length/width ratio) that corresponds to one periodic unit within counter dual-flow PHEs under steady-state and laminar conditions. A relatively generalizable design guideline of fins with convergent-divergent distribution, which can achieve the simultaneous thermo-hydraulic improvement, is generated using a TG and verified with

a series of CFD simulations. Moreover, the underlying mechanisms behind the obtained fin topology are analyzed carefully based on the synergy field theory [33].

2. Problem Formulation of the TG

2.1 Simplification and Assumptions

Due to the massive computational time and cost of the topology generation process, it is difficult to conduct it on an industrial heat exchanger that holds the complicated structure and flow patterns. Accordingly, the 3D industrial PHE is simplified to a 2D counter flow PHE's unit as seen in Fig.1. Based on this simplification, several reasonable assumptions are considered:

(1) The 2D counter flow PHE's unit is insulated, no heat loss to the surrounding
(2) The effect of heat, mass and momentum transfer is neglected in the third direction.
(3) The fluid properties are assumed to be temperature independent
(4) Steady-state conditions

2.2 Conjugate heat transfer modeling

The conjugate heat transfer physics in HXs combines the fluid dynamics and heat transfer models.

2.2.1 Fluid dynamics model

The incompressible and steady-state fluid flow in the HX is modelled using the dimensionless continuity and momentum equations which are given as respectively:

$$\begin{gathered} \nabla^* . \boldsymbol{v}^* = 0 \\ (\boldsymbol{v}^* . \nabla^*)\boldsymbol{v}^* = -\nabla^* P^* + \frac{1}{Re} . \nabla^{*2}\boldsymbol{v}^* - \boldsymbol{f}(\gamma) \end{gathered} \tag{1}$$

where $\boldsymbol{v}^*$ is the dimensionless velocity vector, P^* the dimensionless pressure field, γ is the TG's design variables and Re is the Reynolds number of the topology generation process. The dimensionless variables are defined with respect to the width of the channel denoted as L, and a characteristic speed designated as the inlet velocity v_{in} . These dimensionless variables are determined based on the subsequent

formulations:

$$\nabla^* = L\nabla$$
$$\boldsymbol{v}^* = \frac{\boldsymbol{v}}{v_{in}} \tag{2}$$
$$P^* = \frac{P - P_{out}}{\rho v_{in}^2}$$

where P_{out} is the outlet pressure (Pa) and ρ is the density of the fluid (kg/m^3). Moreover, the Re denotes the ratio between the inertia over the viscous terms defined as:

$$Re = \frac{\rho v_{in} D_h}{\mu} \tag{3}$$

μ is the fluid viscosity and D_h is the hydraulic diameter or characteristic length of the design domain. In the implementation of the density-based topology generation, the Momentum equation needs to be modified by adding a Brinkman friction $\boldsymbol{f}$ coefficient to dominate the design domain treated as porous medium which can be defined as follow:

$$\boldsymbol{f}(\gamma) = \alpha^*(\gamma)\boldsymbol{v}^* \tag{4}$$

where α^* is the dimensionless inverse permeability that must be interpolated between the solid and fluid phases to define the flow path (the detailed interpolation function equations will be discussed in the TG section).

2.2.2 Heat transfer model

The heat transfer is studied in the solids that are dominated by conduction and in the fluids that are dominated by convection. The steady-state dimensionless energy equation is utilized to model the heat transfer of the HX.

$$RePr_f(\boldsymbol{v}^*.\nabla^* T^*) - \nabla^*.(C_k(\gamma)\nabla^* T^*) = 0 \tag{5}$$

where Pr_f is the fluid Prandtl number that represents the ratio of the momentum over the thermal diffusivity, C_k is the thermal conductivity ratio between the solid and fluid phases and T^* is the dimensionless temperature field. The previous mentioned parameters can be expressed as:

where k_f & k_s are the thermal conductivities of the solid and fluid respectively

$$Pr_f = \frac{\mu c_p}{k_f}$$
$$C_k = \frac{k_s}{k_f} \tag{6}$$
$$T^* = \frac{T - T_{in,cold}}{T_{in,hot} - T_{in,cold}}$$

(W/m.K) , c_p is the specific heat of the fluid phase (J/kg.K), μ is the fluid dynamic viscosity (Pa.s) and $T_{in,cold}$, $T_{in,hot}$ are the inlet temperatures of the cold and hot fluid respectively (K).

2.3 Boundary Conditions

As illustrated in Fig.1, a set of Dirichlet boundary conditions are imposed at the inlet of each fluid by setting a uniform velocity and temperature profiles as follow:

$$-\boldsymbol{v}^*.\boldsymbol{n} = 1 \Longleftrightarrow \text{ on } \Gamma_{in,cold} \text{ and } \Gamma_{in,hot}$$
$$T^* = 0 \Longleftrightarrow \text{ on } \Gamma_{in,cold} \tag{7}$$
$$T^* = 1 \Longleftrightarrow \text{ on } \Gamma_{in,hot}$$

where $\boldsymbol{n}$ is the normal vector to the corresponding boundary outwardly oriented to the design domain. Similarly, a uniform pressure and outflow conditions are set at the outlet boundaries of fluid flows as hydraulic and thermal boundary conditions respectively.

$$P^* = 0 \Longleftrightarrow \text{ on } \Gamma_{out,cold} \text{ and } \Gamma_{out,hot}$$
$$-\boldsymbol{n}.\nabla T^* = 0 \Longleftrightarrow \text{ on } \Gamma_{out,cold} \text{ and } \Gamma_{out,hot} \tag{8}$$

The six yellow boundaries of the HX mentioned in the Fig.1 are assumed to be insulated i.e. no heat loss to the surrounding. In addition, a periodic boundary condition is assigned at the top and bottom boundaries of the HX to consider the heat transfer effect from the upper and lower units.

3. Topology generator and CFD Verification

The present section is decomposed into two subsections TG and Computational fluid dynamic (CFD) verification. In the TG subsection, the detailed methodology of the density-based (porosity-based) topology generation process on a dual-flow 2D HX

unit is presented. Thereafter, in the CFD verification section, a set of CFD simulations is carried out on the TG-derived structures to evaluate their thermo-hydraulic performance.

3.1 Topology generator (TG)

3.1.1 Design Parametrization

The density-based parametrization is based on representing the design domain (Fluid channels in the present case) by densities or porosities (design variables) to parametrize the fluid and solid phases. In this study, the initial density distribution has been set to an intermediate design variable, γ_i=0.5, i.e., each mesh element is composed initially of a porous medium that contains 50% fluid and 50% solid. Throughout the topology generation procedure, the density values (γ) can exhibit a continuous variation ranging from 0 (fluid) to 1 (solid). As for the interpolation scheme, the inverse permeability is interpolated between the solid and fluid phases using the following formula [27]:

$$\alpha^*(\gamma) = \alpha^*_{max} * q * \frac{\gamma}{q + 1 - \gamma}$$
$$\alpha^*_{max} = \frac{L\alpha_{max}}{\rho v_{in}} \tag{9}$$

where α^*_{max} is the maximum impermeability value and q is a penalization coefficient. When the value of γ=0, $\alpha \rightarrow 0$, $f \rightarrow 0$, implying that the working fluid, which is the water in the present study, can freely flow through this element and the fluid phase is occupied in this element. By contrast, When the value of γ=1, $\alpha \rightarrow \alpha_{max}$, $f \rightarrow f_{max}$, a huge frictional force is applied on the fluid flow to ensure its zero velocity, which is consistent with the behavior of the solid phase. Concerning the thermal properties interpolation, the thermal conductivity ratio can be interpolated between solid and fluid phases using the classical SIMP (solid isotropic material with penalization) interpolation function [34].

$$C_k(\gamma) = 1 + (C_k - 1)\gamma^p \tag{10}$$

where p is a penalty factor. In order to avoid the mixing of both fluids during the topology generation procedure, the separating solid is considered as fixed solid and excluded from the design domain.

3.1.2 Finite element analysis (FEA)

The governing equations (GEs) presented in Eqs. (1), (5) are discretized in space and solved using Finite element method (FEM). Due to the weak coupling between the two physics (fluid flow and heat transfer), the FEM solver implemented in COMSOL 6.0 is used to sequentially solve the multiphysics problem starting by computing the velocity distribution using Eqs (1) from a pressure initial guess. Then, the velocity field is substituted in the energy equation (Eq.5) to calculate the temperature distribution over the HX. As for the GE's space discretization, a fine mesh with mapped quadratic P1 linear element is built.

3.1.3 Objective and constraints

In this research, the primary objective of the TG is to maximize the thermal effectiveness (ϵ) of the HX, which is defined as the ratio between the actual heat transfer rate to the maximum possible heat transfer rate within the HX, and it can be expressed as [35]:

$$\epsilon = \frac{\left(\dot{m}C_p\right)_{cold} \times \left(T^*_{out,cold} - T^*_{in,cold}\right)}{\left(\dot{m}C_p\right)_{min} \times \left(T^*_{in,hot} - T^*_{in,cold}\right)} \tag{11}$$

where $\dot{m}$ is the mass flow rate (kg/s). The aim of using the maximization of the thermal effectiveness as an objective function of the TG problem arises from its fundamental importance in determining and comparing the thermal performance of the HXs. To constraint the non-linear problem, a set of constraints have been imposed. First, a relaxation is applied on the design variable γ to transform it from discrete to continuous $\gamma \in [0,1]$. Moreover, the governing equations presented in Eqs. (1) & (5) should be also set as a constraint to ensure that their residuals will be zero in each iteration. Eventually, a solid fraction is imposed to constraint the amount of solid generated in the flow channels. Thus, the TG's mathematical problem can be summarized as follows:

$$
\begin{aligned}
&Find\ \ \gamma \\
&Max\ \ \epsilon\ \ (Eq.11) \\
&s.t \begin{cases} 0 \le \gamma \le 1 \\ Eqs.(1),(5) \\ \int_{\Omega} \gamma d\Omega \le v_{fs} \end{cases}
\end{aligned}
\tag{12}
$$

where v_{fs} is the maximum allowed solid volume fraction and Ω is the design domain.

3.1.4 Discrete Adjoint analysis and topology updates

Due to the implicit dependency of the state variables (pressure, velocity and temperature) and the objective function with the design variable, it is impossible to calculate the derivative (sensitivity) of the objective function directly. The discrete adjoint method is used to perform the sensitivity analysis [36]. It consists of transforming the constrained problem into unconstrained by setting up a Lagrangian function that requires the multiplication of the constraints by Lagrange multiplier (adjoint variables):

$$L = \epsilon + \sum_{1}^{n} \lambda_n \varphi_n \tag{13}$$

where *n* is the number of constraints, λ is the adjoint variables and φ corresponds to the left-hand side terms of the constraints in Eq. (12), expressed in the form h(x)=0. Then, the chain rule is used to compute the derivative of the Lagrange function. Posteriorly, the adjoint problem is formulated to compute the adjoint variables. The generation process is carried out using the FEM (Finite element method)-based software COMSOL multiphysics and for the detailed methodology of the discrete adjoint method the readers are referred to Annex A. According to the objective function derivatives, the globally convergent method of moving asymptotes (GCMMA) [37], which is built in the COMSOL software package, is used with 0.1 external move limits to iteratively updates the design variables distribution. The iterative generation process is judged to be converged when the criterion $|L_k - L_{k-1}| < 1 \times 10^{-3}$ is achieved.

3.1.5 Filter and projection

During the topology generation, filters are necessary to avoid the numerical instabilities (checkerboard, mesh dependency, local optimum, etc.) caused by the ill-posedness of the TG problems [38]. To avoid this issue, filters and projection techniques are adopted to control the computed design variables. For the filtering technique, the Helmholtz PDE filter [39] is adopted to obtain an averaged filtered design variables γ_f:

$$\gamma_f = R^2\nabla^2\gamma_f + \gamma \tag{14}$$

where R is the filter radius which is considered as the mesh element size in the current study. After the filtering process, an intermediate density area near the solid-fluid interface is generated. In order to reduce it, the filtered design variables are projected using the smooth Heaviside hyperbolic tangent projection [40]:

$$\gamma_p = \frac{\tanh\left(\beta\left(\gamma_f - \gamma_\beta\right)\right) + \tanh\left(\beta\gamma_\beta\right)}{\tanh\left(\beta\left(1 - \gamma_\beta\right)\right) + \tanh\left(\beta\gamma_\beta\right)} \tag{15}$$

where γ_p is the projected design variable, β is the projection slope and γ_β is the projection point.

3.1.6 Continuation scheme

A continuation strategy is applied on the penalization coefficients (q and p) of the interpolation functions and the projection slope (β). The continuation sequence is chosen to attenuate a possible convergence to a local optimum. The proposed continuation scheme is composed of six steps as shown in Tab.1. For the first three steps, the parameters values are set to low values to stabilize the topology generation process and guarantee better sensitivity scaling by giving the generator some freedom. Then, the parameters values are slowly increased in the last steps to acquire more precise physical models by penalizing the intermediate densities and sharping the interfaces. The continuation strategy leads to better performance and gives more stability to the topology generation process than starting with the final parameters values which often leads to fast convergence to a local optimum in such a non-convex problem [41].

Table 1: Continuation scheme for damping and projection coefficients

Step	1	2	3	4	5	6
q	0.01	0.01	0.01	0.03	0.05	0.1
p	1	1	1	2	3	3
β	1	2	4	4	8	8

3.1.7 TG setting parameters

The values of the TG's input parameters are summarized in the Table 2. First, the Reynolds number (Re) is computed according to the inlet boundaries for simplicity and the hydraulic diameter (D_h) is assumed to be double of the height of an infinite wide channel [42],[43]. The maximum impermeability (α_{max}) is set to 10^4 to avert the convergence difficulties caused by high impermeability values [29], [44]. Additionally, the solid fraction (v_{fs}) in the generation process is set to 0.2 (20%) i.e. the created solids in the flow channels are constraint to 20% of the area of both channels. As mentioned in section 3.1.1, the solid plates (20% of the whole HX area) presented in Fig.1 are excluded from the design domain, thus the total solid fraction (solid generated inside flow channels + three fixed plates) of the HX is 20%+20%=40%. The acquired topology is strongly influenced by the input parameter of the TG [25], emphasizing the high sensitivity of the essential parameters (Re, Pr_f, C_k) of the dimensionless governing equations presented in Eqs. 1&5. A thorough examination of the impact of these parameters on the resulting topology will be extensively discussed in the results section. Eventually, the projection point γ_β of the hyperbolic projection process is set to 0.5.

Table 2: TG parameters

Parameter	Value
Re	200 - 1000
Pr_f	6.85- 600
C_k	50 - 450
α_{max}	10^4
v_{fs}	0.2 (20%)
γ_β	0.5

3.2 Computational Fluid Dynamics (CFD) validation

For the purpose of validating the design methodology and accurately evaluating the thermo-hydraulic performances, a set of computational fluid dynamics (CFD) simulations is conducted on the TG-derived HXs using the FEM solver of COMSOL [42]. The CFD validation analysis is a mandatory stage since the density-based TG is unable to accurately evaluate the performance of the generated topologies due to the governing equations modification, low mesh quality (no boundary layers, fixed mesh) and the existence of intermediate porosities at the solid/fluid interface after achieving the convergence criteria.

3.2.1 Thresholding

At the end of the topology generation process, the interface of the obtained topologies is not clear (pure solid or fluid) and some intermediate densities still exist which hold the non-physical meaning. Therefore, a predefined threshold is applied on the design variable to allow the extraction of the TG-derived HX geometry for verification process. The threshold value (γ_{th}) is taken as 0.5 i.e. 50% of the intermediate densities are taken as solid ($\gamma_{th} \geq 0.5$) and the other 50% as fluid ($\gamma_{th} < 0.5$) [45].

3.2.2 Governing equations

In the CFD validation analysis, the governing equations (1) & (5) are set up without any modification in the momentum equation as in the topology generation, assuming for steady-state and incompressible flow conditions. In conjunction with the previous mentioned equations, the k-ε model is employed to simulate the fluid flow inside the HX in the laminar and turbulent regions. A good mesh quality with eight boundary layers is built to discretize the GEs in space using P1 elements.

3.2.3 Dimensionalization of the HX unit, boundary conditions and physical properties

In order to evaluate the realistic and practical thermo-hydraulic performance, the non-dimensional design domain utilized in TG's section is transformed to a dimensional one by specifying the value of the width of the flow channel to 4 mm. Accordingly, the remaining dimensions of the HX unit are also dimensionalized as

illustrated by Fig.1c. As for the boundary conditions, a uniform velocity and temperature profiles are imposed at the inlets. The inlet temperatures are set to 20℃ and 80℃ for the cold and hot fluid respectively. Moreover, zero outlet pressure with outflow conditions are assigned as outlet hydraulic and thermal boundary conditions respectively. In the current work, the numerical verification process is divided into 2 parts (Case 1&2). Case 1: the thermo-hydraulic performance is evaluated and compared under similar inlet velocity (Re_{hot}=300-3000; Re_{cold}=109.4-1094.5) and fluid material (water) for the cold and hot fluids. Case 2: different inlet velocities ($Re_{cold}/Re_{hot}=10$) with fluid material (cold fluid → water, hot fluid →oil) are assigned for the cold and hot fluid. In both cases, the structures are simulated in the laminar and turbulent regions (Re_{hot}=30-300; Re_{cold}=300-3000). The primary objective behind evaluating the performance of the HX units under varied conditions is to ascertain that the superiority of the proposed design guideline can remain effective in different cases. The water and oil physical properties are considered as temperature dependent using the fitting polynomials given in Table 3. By contrast, the temperature dependence on Aluminum physical properties is ignored as shown in Table 3 below. Furthermore, the expansion characteristics of the solid material are disregarded in our numerical analysis.

Table 3: Physical properties of fluid and solid used for the numerical simulation (283 K <T< 363) *[46], [47]*

Water	*Density [kg.m^{-3}]*	$\rho = -9\times10^{-8}T^4 + 3\times10^{-5}T^3 - 6.8\times10^{-3}T^2 + 2.78T + 1000.2$
	Specific heat [J kg^{-1} K^{-1}]	$C_P = 2\times10^{-6}T^4 - 6\times10^{-4}T^3 + 5.48\times10^{-2}T^2 - 2.18T + 4208.6$
	Viscosity [Pa s]	$\mu = 3\times10^{-11}T^4 - 7\times10^{-9}T^3 + 8\times10^{-7}T^2 - 5\times10^{-5}T + 0.0017$
	Thermal conductivity [W m^{-1} K^{-1}]	$k = -4\times10^{-10}T^4 + 10^{-7}T^3 - 2\times10^{-5}T^2 + 2.5\times10^{-3}T + 0.5557$
Oil	*Density [kg.m^{-3}]*	$\rho = 7.34\times10^{-5}T^2 - 0.639T + 1068.7$
	Specific heat [J kg^{-1} K^{-1}]	$C_P = 0.00115T^2 + 3.476T + 761.4$
	Viscosity [Pa s]	$\mu = 2.48\times10^{-11}T^6 - 5.16\times10^{-8}T^5 + 4.47\times10^{-5}T^4 - 0.02T^3 + 5.36T^2 - 741.17T + 42669.2$
	Thermal conductivity [W m^{-1} K^{-1}]	$k = 1.54\times10^{-7}T^2 - 2.063\times10^{-4}T + 0.192$
Aluminum	Density [kg.m^{-3}]	$\rho = 2700$
	Specific heat [J kg^{-1} K^{-1}]	$C_P = 900$
	Thermal conductivity [W m^{-1} K^{-1}]	$k = 237$

3.2.4 Mesh dependency

A mesh dependency study is executed to ensure the reliability of the numerical simulation. First, a coarse mesh is built to discretize the HX unit. Then, the mesh is refined by a certain factor following the methodology proposed by Celik et al. [48] until

the after-mentioned stopping criteria is satisfied:

$$Er(\Delta P) = \left|\frac{\Delta P^{k} - \Delta P^{k+1}}{\Delta P^{k}}\right| < 2\% \;\; \& \;\; Er(T_{out}) = \left|\frac{T^{k}_{out,cold} - T^{k+1}_{out,cold}}{T^{k}_{out,cold}}\right| < 2\% \qquad (16)$$

where k is the index of the mesh dependency test, ΔP is the total pressure drop (Pa), $T_{out,cold}$ is the cold flow outlet temperature (°C) and Er is the relative error. As an example, for Re_{hot} = 3000 (Re_{cold} = 1094.5), the details about the mesh dependency study are given in Table 3. As seen that the numerical results become mesh independent when the number of elements hit 1257338.

Table 4: Mesh dependency test at Re_{hot} = 3000

Elements number	ΔP (Pa)	Error (ΔP) (%)	$T_{out,cold}$ (°C)	Error $(T_{out,cold})$ (%)
201455	418.2	--	32.5	--
581295	390	7.2%	30.8	5.51%
1257338	373.2	4.5%	29.88	3.07%
3125008	369.03	1.07%	29.7	0.6%

3.2.5 Theoretical verification

In order to validate the accuracy of the numerical results, we perform a comparative analysis between the computed numerical Nusselt number (Nu) and friction coefficient (f), obtained through the COMSOL solver for the bare HX unit depicted in Figure 8e, with their corresponding theoretical values calculated employing the Sieder-Tate Nusselt number correlation [49] and the friction coefficient correlation for parallel plates [50], as described below:

$$Nu = 1.86 \times Re^{\frac{1}{3}} \times Pr^{\frac{1}{3}} \times \left(\frac{D_h}{l}\right)^{1/3} \times \left(\frac{\mu_b}{\mu_w}\right)^{0.14}$$
$$f = \frac{96}{Re} \qquad (17)$$

where μ_b is the viscosity at the bulk mean temperature (Pa.s), μ_w is the viscosity at the wall temperature (Pa.s), l is the length of the HX unit (m). Figure 2 clearly demonstrates a significant level of congruity between the numerical and the correlated results.

4. Results and Discussions

4.1 TG-results and the influence of parameters

4.1.1 Influence of Re , Pr_f & C_k

We investigate firstly the effect of the three essential parameters in the dimensionless TG represented by *Re,* Pr_f & C_k. By increasing the *Re* & Pr_f, the convective term in the energy equation is intensified, thereby causing an increase in the minimum width of the flow channels, as illustrated in Figures 3 & 4. This elucidates that with the increase of the convection term, the flow force exceeds the force exerted by the appeared solids (from top and bottom of the flow channel), resulting in an unhindered fluid flow through the channel. In contrast, elevating the conduction term of the energy equation through an increase of the thermal conductivity ratio (C_k) results in a reduction of the minimal distance of the flow channel as depicted by Fig 5. This implies that as the conduction term increases, the generated solids attempt to block the fluid flow by impeding its passage. It is noteworthy to mention that an increase in the C_k results in a proportional increase in thermal conductivity of the solid phase, whereas the thermal conductivity of the fluid phase remains unchanged even with the increase of C_k.

All topologies depicted in the previous figures show the irregular fin geometries emerged along the solid wall, the symmetry about the vertical axis at the middle of the HX unit. And most importantly, the convergent-divergent arrangement feature i.e. the height and width of the fins increase gradually until the center of the HX unit and then it decreases.

4.1.2 Influence of dissimilar fluid material and inlet velocity

The previous topologies are acquired using the same fluid material and inlet velocity for the hot and cold fluids. To observe whether the features will be conserved under different conditions, dissimilar fluid material (Pr_{cold} = 6.85 & Pr_{hot} = 364) and inlet velocities are imposed for the cold and hot fluids. As exemplified by Fig 6, the symmetry is disrupted while the irregular and C-D distribution features are maintained under different Reynolds number ratio between the cold and hot fluids. The Reynolds number ratio should be also carefully set, beyond the defined range in Fig6 for the

prescribed values of Pr_f (Pr_{cold}=6.85 (water) & Pr_{hot}=364 (oil)) and C_k (C_{kcold}=25, C_{khot} =150), the blocking issues will occurs in the cold or hot fluid channels. This blocking phenomenon can be attributed to the disparity in convective heat transfer rates between channels, where a higher rate in one channel leads to an increase in the minimal distance and then decrease in the amount of solid within that channel. Concurrently, to maintain the imposed solid fraction within the flow channels during the topology generation, a compensatory increase in solid content must occur in the other channel leading to a decrease in the minimal distance and then the blocking of the channel.

4.1.3 Influence of initial topology

In the topology generation, the initial guess holds significant importance as it directly influences the obtained results. Correspondingly, two different initial densities distribution using rectangular and circular fins are suggested instead of starting with a uniform density distribution as the topologies acquired previously. As illustrated by Fig 7, all acquired topologies using rectangular and circular fins as initial guess possess the C-D distribution features with a remarkable difference in the acquired fins distribution. Numerically, a marginal difference of 0.06% has been observed in the optimal value of the objective function when employing initially rectangular and circular fins, in comparison to the result obtained using a uniform initial density distribution. The difference in the optimum value is negligible and may be explained by the utilization of the continuation scheme in topology generation that can leads to maximized performance for different initial setting.

4.1.4 Summarization and discussion

In summary, the acquired topologies by the TG are strongly affected by the input parameters, which is a common issue for heat transfer TO [32]. Hence, a limitation of setting for a compromise between convection and conduction terms should be considered. Surpassing the limited ranges of parameters inevitably leads to the emergence of flow channel's blocking issues. Additionally, the C-D distribution feature is conserved irrespective of the prevailing conditions while the symmetry feature is lost when fluid material and the inlet Reynolds number are changed for the cold and hot fluids.

4.2 Convergent divergent design and performance comparison using CFD

4.2.1 Investigated HX units

The two TG-derived HX units presented in Fig 3c & 4b are randomly selected as benchmarks for the numerical comparison stage (cases 1&2) and named TG-HX1 and TG-HX2 respectively. For more consistency between the TG and the case 2 (different fluids: water-oil and inlet conditions: $Re_{cold}/Re_{hot}=10$) of the CFD analysis, the TG-derived HX under different fluid material (Pr_{cold}=6.85, Pr_{hot}=364) and different inlet conditions ($Re_{cold}/Re_{hot}=10$) presented in figure 6.a is selected for the CFD investigation stage under case 2 conditions and named TG-HX3. Moreover, a HX unit with conventional fin design (Constant fin height 1 mm and width 5 mm) having rectangular shapes (as illustrated by Fig 8d) is introduced to compare its thermo-hydraulic performance with the TG-acquired HX units. To make a fair comparison, all HX units have the same solid fraction (36%), boundary conditions and dimensions. The investigated HX units are presented in Fig 8.

4.2.2 The convergent-divergent design

Taking the inspiration from the topology generated fins that are mainly featured by the convergent-divergent distribution, a simplified HX unit with convergent-divergent arrangement of fins is designed with a minimal channel height (1.3 mm) using analogous rectangular shapes of the conventional design as seen in Fig. 8c.

4.2.3 Parameters definition for thermo-hydraulic performance evaluation

For the purpose of evaluating the thermal performance of the HXs, the Nusselt number (*Nu*) that represents the convective over the conduction heat transfer in the fluid is selected as criteria and evaluated using the following equation:

$$Nu = \frac{hD_h}{k_f} \tag{18}$$

where h is the convective heat transfer coefficient (W/m^{2}K) and k_f is the fluid thermal conductivity (W/mK). As demonstrated by Fig 9a, The Nusselt number exhibits an improvement in the TG-derived and simplified HX units compared to the conventional one, across a broad range of Reynolds number in both cases 1 and 2. This enhancement can be elucidated by the augmentation of local flow velocity within the

TG-acquired and simplified HX flow channels when compared with the local flow velocity within the channels of the conventional HX. Subsequently, this will leads to an intensification of the convective heat transfer coefficient h and then the improvement of the Nu.

To assess the hydraulic performance of the HX units, the friction coefficient is evaluated for all HX units using the Darcy–Weisbach equation presented as follow [51]:

$$f = \frac{2\Delta P D_h}{\rho v_{in}^2 l} \tag{19}$$

Fig. 9b exemplifies that the friction coefficient of the generated and simplified HX units is higher compared to the conventional one. The observed augmentation in the friction coefficient can be attributed to the presence of several tiny fins structures inside generated structures, as well as to the disparity of the minimal distance inside the flow channels for the TG-derived and simplified HX units compared to the conventional design.

To consider the thermal and hydraulic performance simultaneously, the PEC (performance evaluation criteria) which fractionally combine the Nusselt number with friction coefficient is evaluated for the three HX units. As seen in Eq. 20, the friction coefficient undergoes an exponentiation of 1/3 as prescribed by the methodology of Webb and Eckert [52].

$$PEC = \frac{Nu/Nu_0}{(f/f_0)^{1/3}} \tag{20}$$

where the Nu_0 and f_0 are the Nusselt number and the friction coefficient for the Conventional HX. The thermo-hydraulic performance of the TG-derived and simplified HXs surpasses that of the conventional one under a broad range of Reynolds numbers, as illustrated in Figure 9c. This superiority of the TG-acquired and simplified HX units is observed in both cases 1 and 2 with enhancement up to 22.5% and 9.7% and up to 36.11% and 16.08%, respectively.

4.3 Physical interpretation

Figure 10 depicts (a) the normalized velocity contours, (b) the normalized velocity, (c) the normalized local pressure gradient, (d) the normalized local heat transfer coefficient over the TG-HX1 at Re_{hot}=300. The flow channels inside the TG-HX1 are decomposed into two sections (Convergent and divergent). In the convergent section,

the current fin distribution attempts to gradually increase the convective heat transfer by increasing the velocity of the fluid resulting in an augmentation of the local heat transfer coefficient and pressure drop. Thereafter, in the divergent section, the generated design seeks to progressively decrease the fluid velocity, which will simultaneously reduce the local pressure drop and heat transfer coefficient. The proportional variation of the local heat transfer coefficient and pressure drop with respect to the velocity behavior could be proved and confirmed by the following equations [51]:

$$\Delta P = \frac{f \rho v_{in}^2 l}{2 D_h}$$
$$h = \frac{k_f Nu}{D_h} \quad \leftrightarrow \quad Nu \propto v \tag{21}$$

As presented in Eq. 21, the variation of pressure drop is proportional to the magnitude of velocity. Similarly, the heat transfer coefficient is commensurable with the Nusselt number, which is correlated to the velocity. Apparently, the TG-derived design of fins intensifies the convective thermal performance of the HX unit in the convergent section and improves its hydraulic performance in the divergent section for the purpose of achieving the simultaneous thermo-hydraulic enhancement. Besides, regarding the fluctuations in all plots, this could be explained by the flow disturbance and eddies generated inside the channels.

Additionally, one of the most important parameters to evaluate the convective heat transfer is the included angle between the velocity vector and the temperature gradient [53]–[57]. By referring to the dimensionless energy equation presented in Eq. 5, increasing the *Re* or Pr_f will directly enhance the heat transfer which has been considered as a classical and well known method in the literature to enhance the heat transfer. In fact, increasing the dot product of the velocity and temperature gradient ($\boldsymbol{v}.\boldsymbol{\nabla T}$) could also magnify the heat transfer. Therefore, the synergy field number of the included angle could be expressed as:

$$\cos\theta = \frac{\boldsymbol{v}.\boldsymbol{\nabla T}}{\|\boldsymbol{v}\| \times \|\boldsymbol{\nabla T}\|} \tag{22}$$

where θ is the incident angle between $\boldsymbol{v}$ and $\boldsymbol{\nabla T}$ are the velocity and temperature gradient vectors respectively, $\|\boldsymbol{v}\|$ and $\|\boldsymbol{\nabla T}\|$ are the magnitude of the velocity and

temperature gradient vectors, respectively. Figure 11a demonstrates that the absolute value of the synergy field number $|cos\theta|$ is locally increased thanks to the created vortex (Flow swirls) between the generated fins. Besides, Figure 11b illustrates that the absolute value of the averaged synergy field number for the TG-generated and simplified HX units are larger than the conventional one under a wide range of Re. It is important to note that the synergy field is employed in this subsection as a supplementary interpretive indicator rather than a definitive tool to interpret the convective heat transfer phenomena and heat transfer enhancement in HXs. This is due to the fact that the convective heat transfer phenomena is governed by several physical parameters and not solely by the velocity.

4.4 Incompatibility of velocity fields between CFD and TG

The C-D design derived from the TG is proven of good thermal-hydraulic performance in terms of the CFD and physical analysis. However, the incompatibility of velocity fields between CFD and topology generation is found as shown in Fig 12.

The observation reveals an important velocity in the solid phase as seen in Figure 12 of the generated topology depicted in Fig.7b, elucidating that the maximal imposed impermeability (which has been utilized in literature for conjugate heat transfer TO [29], [30], [42], [58]) was insufficient to enforce zero velocities for the solid phase. This insufficiency may be attributed to the employment of a restricted design domain in the topology generation process.

Accordingly, the acquired results could be considered as a novel generated topology rather than an optimized one, while concurrently emphasizing the improvement of the thermo-hydraulic performance resulted from the utilization of the newly generated C-D fins.

For future work, to address the solid-phase velocity artifacts associated with the density-based topology generation, it is essential to employ a higher maximum impermeability value [59]. This adjustment will enhance the penalization capability of the impermeability interpolation function for the solid-phase velocity during the optimization process, thereby preventing the occurrence of non-physical velocity artifacts in the solid phase.

5. Conclusions and Perspectives

In this research, a novel fin design with convergent-divergent distribution is generated by using a gradient-based TG. An in-depth examination is carried out to explore the influence of the TG's essential parameters (*Re, Pr_f, C_k*) on the resulted topologies. According the investigation stage, when the convective heat transfer is increased by increasing the *Re & Pr_f,* the minimal distance inside the channels increases simultaneously leading to an unhindered flow of the fluid inside the channels. Conversely, when the conduction term is increased by increasing the C_k, the appeared solid tends to obstruct the fluid passage inside the channels. Accordingly, a trade-off between conduction and convection is crucial to avoid the occurrence of fluid passage blockages within the channels. Under the different input parameter settings, the TG-derived geometries are in form of fins and featured essentially by the convergent-divergent distribution along the length of the HX.

Inspired from the preceding feature, a convergent-divergent fin distribution is designed using rectangular shapes. The aim behind introducing such design is to provide a novel guideline for fin design following the essential topological feature with rectangular shapes that could be easy manufactured even with conventional techniques. Moreover, a conventional fin design with uniform distribution is also introduced for comparison. CFD analysis is executed under two different cases (1&2) on four HX units with two TG-derived, one simplified and one conventional designs to compare numerically their thermo-hydraulic performance. Under the same Reynolds number, the TG-acquired and simplified HX units have better thermal performance compared to the HX unit with conventional fins: Nusselt number increase up to 46%, 14% for case1 and 56.16%, 17.68% for case 2, respectively. To characterize the thermal and hydraulic performance simultaneously, the PEC is evaluated for all HX units. It is identified that the advantage of the TG-acquired and simplified HX units over the conventional one with thermo-hydraulic improvement up to 22.5%, 9.7% for case 1 and 36%, 16% for case 2, respectively. The diminishment in performance enhancement observed between the TG-obtained and simplified HXs might be attributed to the omission of several topological features during the design of the simplified HX.

A detailed physical interpretation of this novel fin design guideline is provided by analyzing the local velocity, pressure drop, heat transfer coefficient and synergy field with respect to the HX unit's length. The fins can increase the local velocity in the

convergent section and decrease it in the divergent section leading to a proportional variation of the local pressure drop and heat transfer coefficient along the HX unit with the local augmentation of synergy field number between the fins.

Lastly, an issue has been identified in the obtained topologies following an examination of the velocity distribution. The deficiency in impermeability intensity is evident, as it fails to enforce a zero velocity for the solid phase.

As for the future work, we will validate this newly-proposed fin design guideline in experiments. Additionally, the extension of the method to handle 3D HXs could be also another research topic. An important additional future direction is the experimental validation of the C-D design of fins, which involves assessing the manufacturability of such new design of fins and providing a comparison between numerical and experimental results to validate our numerical model.

Annex A: Discrete Adjoint Method

Due to the implicit dependency of the state variables (pressure, velocity and temperature) and the objective function with the design variable, it is impossible to calculate the derivative (sensitivity) of the objective function directly. The discrete adjoint method is used to perform the sensitivity analysis [36]. It consists of transforming the constrained problem into unconstrained by setting up a Lagrangian function that requires the multiplication of the constraints by Lagrange multiplier (adjoint variables):

$$L = \epsilon + \lambda_u^{\mathrm{T}} \varphi_u + \lambda_T^{\mathrm{T}} \varphi_T \tag{A1}$$

where φ_u and φ_T are the residuals of the momentum and energy equations respectively, λ_u and λ_T are the adjoint variables vector. The total derivative of the lagrangian function with respect to the design variables (γ) can be written as follows:

$$\frac{dL}{d\gamma} = \frac{d\epsilon}{d\gamma} + \lambda_u^{\mathrm{T}} \frac{d\varphi_u}{d\gamma} + \lambda_T^{\mathrm{T}} \frac{d\varphi_T}{d\gamma} \tag{A2}$$

Then, the chain rule is used to compute the derivative of the Lagrange function:

$$\begin{aligned} \frac{dL}{d\gamma} = \frac{d\epsilon}{d\gamma} + \lambda_u^{\mathrm{T}} \frac{d\varphi_u}{d\gamma} + \lambda_T^{\mathrm{T}} \frac{d\varphi_T}{d\gamma} + \left(\frac{d\epsilon}{du} + \lambda_u^{\mathrm{T}} \frac{d\varphi_u}{du}\right) \frac{du}{d\gamma} \\ + \left(\frac{d\epsilon}{dT} + \lambda_T^{\mathrm{T}} \frac{d\varphi_T}{dT}\right) \frac{dT}{d\gamma} \end{aligned} \tag{A3}$$

The discrete adjoint approach assumes the verification of the adjoint vector with the

equation multiplied by $\frac{du}{d\gamma}$ and $\frac{dT}{d\gamma}$, to avoid the computation of such difficult terms. Accordingly, the adjoint equations can be formulated as follow:

$$\left(\frac{d\varphi_T}{dT}\right)^{\mathrm{T}} \lambda_T = \left(-\frac{d\epsilon}{dT}\right)^{\mathrm{T}}$$
$$\left(\frac{d\varphi_u}{du}\right)^{\mathrm{T}} \lambda_u = -\left[\left(\frac{d\epsilon}{du}\right)^{\mathrm{T}} + \left(\frac{d\varphi_T}{du}\right)^{\mathrm{T}} \lambda_T\right] \quad \text{(A4)}$$

Upon the computation of the adjoint variables (λ_u,λ_T) through the aforementioned adjoint equations (Eq. A4), the sensitivities of the objective function can be directly assessed using Equation A2. Furthermore, the sensitivities computed are subsequently projected back, employing the chain rule also in this process:

$$\frac{d\epsilon}{d\gamma} = \frac{d\epsilon}{d\gamma} + \frac{d\epsilon}{d\gamma_p}\frac{d\gamma_p}{d\gamma_f}\frac{d\gamma_f}{d\gamma} \quad \text{(A5)}$$

where γ_f and γ_p are the filtered and projected design variables. The $\frac{d\gamma_p}{d\gamma_f}$ term of Eq. A5 is determined through the differentiation of the hyperbolic projection equation (Equation 15) of section 3.1.5.

Acknowledgements

This work is financially supported by Région Pays de la Loire within the NExT2Talents program TOP-OPTIM project (998UMR6607 EOTP NEXINTERTALENTHUA).

Declaration of interests

The authors declare that they have no known competing financial interests or personal relationships that could have appeared to influence the work reported in this paper.

References

[1] L. Luo et al., 'Design, Fabrication And Experimental Study Of New Compact Mini Heat-Exchangers', in *Microreaction Technology*, M. Matlosz, W. Ehrfeld, and J. P. Baselt, Eds. Berlin, Heidelberg: Springer Berlin Heidelberg, 2001, pp. 68–69[Online]. Availablehttp://link.springer.com/10.1007/978-3-642-56763-6_7[Accessed: 26September2022].

[2] L. Luo et al., 'Heat exchanger: from micro- to multi-scale design optimization', *Int. J. Energy Res.*, vol. 31, no. 13, pp. 1266–1274, Oct. 2007 [Online]. Available: 10.1002/er.1298.

[3] Q. Li et al., 'Compact heat exchangers: A review and future applications for a new generation of high temperature solar receivers', *Renewable and Sustainable Energy Reviews*, vol. 15, no. 9, pp. 4855–4875, Dec. 2011 [Online]. Available: 10.1016/j.rser.2011.07.066.

[4] M. M. Aslam Bhutta et al., 'CFD applications in various heat exchangers design: A review', *Applied Thermal Engineering*, vol. 32, pp. 1–12, Jan. 2012 [Online]. Available: 10.1016/j.applthermaleng.2011.09.001.

[5] C. Kandilli and A. Koclu, 'Assessment of the optimum operation conditions of a plate heat exchanger for waste heat recovery in textile industry', *Renewable and Sustainable Energy Reviews*, vol. 15, no. 9, pp. 4424–4431, Dec. 2011 [Online]. Available: 10.1016/j.rser.2011.07.110.

[6] H. Ma et al., 'Assessment of the optimum operation conditions on a heat pipe heat exchanger for waste heat recovery in steel industry', *Renewable and Sustainable Energy Reviews*, vol. 79, pp. 50–60, Nov. 2017 [Online]. Available: 10.1016/j.rser.2017.04.122.

[7] Y. Li et al., 'Tailoring the fluid flow distribution in a parallel mini-channel heat sink under multiple-peak heat flux', *Thermal Science and Engineering Progress*, vol. 29, p. 101182, Mar. 2022 [Online]. Available: 10.1016/j.tsep.2021.101182.

[8] Z. Taghizadeh-Tabari et al., 'The study on application of TiO 2 /water nanofluid in plate heat exchanger of milk pasteurization industries', *Renewable and Sustainable Energy Reviews*, vol. 58, pp. 1318–1326, May 2016 [Online]. Available: 10.1016/j.rser.2015.12.292.

[9] T. Alam and M.-H. Kim, 'A comprehensive review on single phase heat transfer enhancement techniques in heat exchanger applications', *Renewable and Sustainable Energy Reviews*, vol. 81, pp. 813–839, Jan. 2018 [Online]. Available: 10.1016/j.rser.2017.08.060.

[10] P. Pongsoi et al., 'Heat transfer and flow characteristics of spiral fin-and-tube heat exchangers: A review', *International Journal of Heat and Mass Transfer*, vol. 79, pp. 417–431, Dec. 2014 [Online]. Available: 10.1016/j.ijheatmasstransfer.2014.07.072.

[11] A. A. Bhuiyan and A. K. M. S. Islam, 'Thermal and hydraulic performance of finned-tube heat exchangers under different flow ranges: A review on modeling and experiment', *International Journal of Heat and Mass Transfer*, vol. 101, pp. 38–59, Oct. 2016 [Online]. Available: 10.1016/j.ijheatmasstransfer.2016.05.022.

[12] M. M. Abu-Khader, 'Plate heat exchangers: Recent advances', *Renewable and Sustainable Energy Reviews*, vol. 16, no. 4, pp. 1883–1891, May 2012 [Online]. Available: 10.1016/j.rser.2012.01.009.

[13] L. Wang et al., *Plate heat exchangers: design, applications and performance*. Southampton: WIT Press, 2007.

[14] E. M. Sparrow and S. H. Lin, 'Heat-transfer characteristics of polygonal and plate fins',

International Journal of Heat and Mass Transfer, vol. 7, no. 8, pp. 951–953, Aug. 1964 [Online]. Available: 10.1016/0017-9310(64)90150-4.

[15] H. Zabronsky, 'Temperature Distribution and Efficiency of a Heat Exchanger Using Square Fins on Round Tubes', *Journal of Applied Mechanics*, vol. 22, no. 1, pp. 119–122, Mar. 1955 [Online]. Available: 10.1115/1.4010981.

[16] J.-Y. Jang et al., 'The thermal-hydraulic characteristics of staggered circular finned-tube heat exchangers under dry and dehumidifying conditions', *International Journal of Heat and Mass Transfer*, vol. 41, no. 21, pp. 3321–3337, Nov. 1998 [Online]. Available: 10.1016/S0017-9310(98)00037-4.

[17] S. Sanaye and H. Hajabdollahi, 'Thermal-economic multi-objective optimization of plate fin heat exchanger using genetic algorithm', *Applied Energy*, vol. 87, no. 6, pp. 1893–1902, Jun. 2010 [Online]. Available: 10.1016/j.apenergy.2009.11.016.

[18] H. Nemati et al., 'Shape optimisation of air-cooled finned-tube heat exchangers', *International Journal of Thermal Sciences*, vol. 150, p. 106233, Apr. 2020 [Online]. Available: 10.1016/j.ijthermalsci.2019.106233.

[19] L. Luo, Ed., *Heat and Mass Transfer Intensification and Shape Optimization*. London: Springer London, 2013[Online]. Availablehttp://link.springer.com/10.1007/978-1-4471-4742-8[Accessed: 6November2021].

[20] M. Yang et al., 'Experimental study on single-phase hybrid microchannel cooling using HFE-7100 for liquid-cooled chips', *International Journal of Heat and Mass Transfer*, vol. 160, p. 120230, Oct. 2020 [Online]. Available: 10.1016/j.ijheatmasstransfer.2020.120230.

[21] T. Dbouk, 'A review about the engineering design of optimal heat transfer systems using topology optimization', *Applied Thermal Engineering*, vol. 112, pp. 841–854, Feb. 2017 [Online]. Available: 10.1016/j.applthermaleng.2016.10.134.

[22] J. Alexandersen and C. S. Andreasen, 'A Review of Topology Optimisation for Fluid-Based Problems', *Fluids*, vol. 5, no. 1, p. 29, Mar. 2020 [Online]. Available: 10.3390/fluids5010029.

[23] A. Fawaz et al., 'Topology optimization of heat exchangers: A review', *Energy*, p. 124053, Apr. 2022 [Online]. Available: 10.1016/j.energy.2022.124053.

[24] H. Li et al., 'Optimal design and thermal modelling for liquid-cooled heat sink based on multi-objective topology optimization: An experimental and numerical study', *International Journal of Heat and Mass Transfer*, vol. 144, p. 118638, Dec. 2019 [Online]. Available: 10.1016/j.ijheatmasstransfer.2019.118638.

[25] H. Kobayashi et al., 'Freeform winglet design of fin-and-tube heat exchangers guided by topology optimization', *Applied Thermal Engineering*, vol. 161, p. 114020, Oct. 2019 [Online]. Available: 10.1016/j.applthermaleng.2019.114020.

[26] T. Zeng et al., 'Topology optimization of heat sinks for instantaneous chip cooling using a transient pseudo-3D thermofluid model', *International Journal of Heat and Mass Transfer*, vol. 154, p. 119681, Jun. 2020 [Online]. Available: 10.1016/j.ijheatmasstransfer.2020.119681.

[27] P. Papazoglou, 'Topology Optimization of Heat Exchangers', Master's thesis, Delft University of Technology, 2015.

[28] R. Tawk et al., 'Topology optimization of heat and mass transfer problems in two fluids—one solid domains', *Numerical Heat Transfer, Part B: Fundamentals*, vol. 76, no. 3, pp. 130–151, Sep. 2019 [Online]. Available: 10.1080/10407790.2019.1644919.

[29] H. Kobayashi et al., 'Topology design of two-fluid heat exchange', *Struct Multidisc Optim*, vol. 63, no. 2, pp. 821–834, Feb. 2021 [Online]. Available: 10.1007/s00158-020-02736-8.

[30] L. C. Høghøj et al., 'Topology optimization of two fluid heat exchangers', *International Journal of Heat and Mass Transfer*, vol. 163, p. 120543, Dec. 2020 [Online]. Available: 10.1016/j.ijheatmasstransfer.2020.120543.
[31] M. Petrovic et al., 'Numerical and experimental performance investigation of a heat exchanger designed using topologically optimized fins', *Applied Thermal Engineering*, vol. 218, p. 119232, Jan. 2023 [Online]. Available: 10.1016/j.applthermaleng.2022.119232.
[32] Y. Hua et al., 'Heat spreading effect on the optimal geometries of cooling structures in a manifold heat sink', *Energy*, vol. 308, p. 132948, Nov. 2024 [Online]. Available: 10.1016/j.energy.2024.132948.
[33] W.-Q. Tao et al., 'A comprehensive review and comparison on heatline concept and field synergy principle', *International Journal of Heat and Mass Transfer*, vol. 135, pp. 436–459, Jun. 2019 [Online]. Available: 10.1016/j.ijheatmasstransfer.2019.01.143.
[34] M. P. Bendsøe, 'Optimal shape design as a material distribution problem', *Structural Optimization*, vol. 1, no. 4, pp. 193–202, Dec. 1989 [Online]. Available: 10.1007/BF01650949.
[35] K. Thulukkanam, *Heat Exchanger Design Handbook*, 0 ed. CRC Press, 2013[Online]. Availablehttps://www.taylorfrancis.com/books/9781439842133[Accessed: 12February2023].
[36] M. B. Giles and N. A. Pierce, 'An Introduction to the Adjoint Approach to Design', *Flow, Turbulence and Combustion*, vol. 65, no. 3/4, pp. 393–415, 2000 [Online]. Available: 10.1023/A:1011430410075.
[37] K. Svanberg, 'A Class of Globally Convergent Optimization Methods Based on Conservative Convex Separable Approximations', *SIAM J. Optim.*, vol. 12, no. 2, pp. 555–573, Jan. 2002 [Online]. Available: 10.1137/S1052623499362822.
[38] O. Sigmund and J. Petersson, 'Numerical instabilities in topology optimization: A survey on procedures dealing with checkerboards, mesh-dependencies and local minima', *Structural Optimization*, vol. 16, no. 1, pp. 68–75, Aug. 1998 [Online]. Available: 10.1007/BF01214002.
[39] B. S. Lazarov and O. Sigmund, 'Filters in topology optimization based on Helmholtz-type differential equations', *Int. J. Numer. Meth. Engng.*, vol. 86, no. 6, pp. 765–781, May 2011 [Online]. Available: 10.1002/nme.3072.
[40] F. Wang et al., 'On projection methods, convergence and robust formulations in topology optimization', *Struct Multidisc Optim*, vol. 43, no. 6, pp. 767–784, Jun. 2011 [Online]. Available: 10.1007/s00158-010-0602-y.
[41] J. Alexandersen et al., 'Large scale three-dimensional topology optimisation of heat sinks cooled by natural convection', *International Journal of Heat and Mass Transfer*, vol. 100, pp. 876–891, Sep. 2016 [Online]. Available: 10.1016/j.ijheatmasstransfer.2016.05.013.
[42] X. Han et al., 'Topology optimization for spider web heat sinks for electronic cooling', *Applied Thermal Engineering*, vol. 195, p. 117154, Aug. 2021 [Online]. Available: 10.1016/j.applthermaleng.2021.117154.
[43] F. A. S. Mota et al., 'Modeling and Design of Plate Heat Exchanger', in *Heat Transfer Studies and Applications*, M. S. N. Kazi, Ed. InTech, 2015[Online]. Availablehttp://www.intechopen.com/books/heat-transfer-studies-and-applications/modeling-and-design-of-plate-heat-exchanger[Accessed: 3May2022].
[44] S. Sun et al., '3D topology optimization of heat sinks for liquid cooling', *Applied Thermal Engineering*, vol. 178, p. 115540, Sep. 2020 [Online]. Available:

10.1016/j.applthermaleng.2020.115540.
[45] S. B. Dilgen et al., 'Density based topology optimization of turbulent flow heat transfer systems', *Struct Multidisc Optim*, vol. 57, no. 5, pp. 1905–1918, May 2018 [Online]. Available: 10.1007/s00158-018-1967-6.
[46] 'IAPWS (2016). Revised release on the IAPWS formulation 1995 for the thermodynamic properties of ordinary water substance for general and scientific use.' .
[47] 'COMSOL Multiphysics® v. 6.1. www.comsol.com. COMSOL AB, Stockholm, Sweden'. .
[48] I. B. Celik et al., 'Procedure for Estimation and Reporting of Uncertainty Due to Discretization in CFD Applications', *J. Fluids Eng.*, vol. 130, no. 7, p. 078001, 2008 [Online]. Available: 10.1115/1.2960953.
[49] J. R. Welty, Ed., *Fundamentals of momentum, heat, and mass transfer*, 5. ed. Hoboken, NJ: Wiley, 2008.
[50] M. Cavazzuti et al., 'Compressible Fanno flows in micro-channels: An enhanced quasi-2D numerical model for laminar flows', *Thermal Science and Engineering Progress*, vol. 10, pp. 10–26, May 2019 [Online]. Available: 10.1016/j.tsep.2019.01.003.
[51] S. Zeng et al., 'Experimental and numerical investigation of a mini channel forced air heat sink designed by topology optimization', *International Journal of Heat and Mass Transfer*, vol. 121, pp. 663–679, Jun. 2018 [Online]. Available: 10.1016/j.ijheatmasstransfer.2018.01.039.
[52] R. L. Webb and E. R. G. Eckert, 'Application of rough surfaces to heat exchanger design', *International Journal of Heat and Mass Transfer*, vol. 15, no. 9, pp. 1647–1658, Sep. 1972 [Online]. Available: 10.1016/0017-9310(72)90095-6.
[53] Z. Y. Guo et al., 'A novel concept for convective heat transfer enhancement', *International Journal of Heat and Mass Transfer*, vol. 41, no. 14, pp. 2221–2225, Jul. 1998 [Online]. Available: 10.1016/S0017-9310(97)00272-X.
[54] W.-Q. Tao et al., 'Field synergy principle for enhancing convective heat transfer—its extension and numerical verifications', *International Journal of Heat and Mass Transfer*, vol. 45, no. 18, pp. 3849–3856, Aug. 2002 [Online]. Available: 10.1016/S0017-9310(02)00097-2.
[55] Z. Y. Guo et al., 'The field synergy (coordination) principle and its applications in enhancing single phase convective heat transfer', *International Journal of Heat and Mass Transfer*, vol. 48, no. 9, pp. 1797–1807, Apr. 2005 [Online]. Available: 10.1016/j.ijheatmasstransfer.2004.11.007.
[56] J. Guo et al., 'The application of field synergy number in shell-and-tube heat exchanger optimization design', *Applied Energy*, vol. 86, no. 10, pp. 2079–2087, Oct. 2009 [Online]. Available: 10.1016/j.apenergy.2009.01.013.
[57] T. Zhao et al., 'Irreversibility evaluation for transport processes revisited', *International Journal of Heat and Mass Transfer*, vol. 189, p. 122699, Jun. 2022 [Online]. Available: 10.1016/j.ijheatmasstransfer.2022.122699.
[58] E. M. Dede, 'Optimization and Design of a Multipass Branching Microchannel Heat Sink for Electronics Cooling', *Journal of Electronic Packaging*, vol. 134, no. 4, p. 041001, Dec. 2012 [Online]. Available: 10.1115/1.4007159.
[59] A. Fawaz et al., 'Topology optimization for dual-flow heat exchangers of moderate conductive material within a narrow design domain: Numerical and experimental investigations', *Applied Thermal Engineering*, vol. 269, p. 125958, Jun. 2025 [Online]. Available: 10.1016/j.applthermaleng.2025.125958.

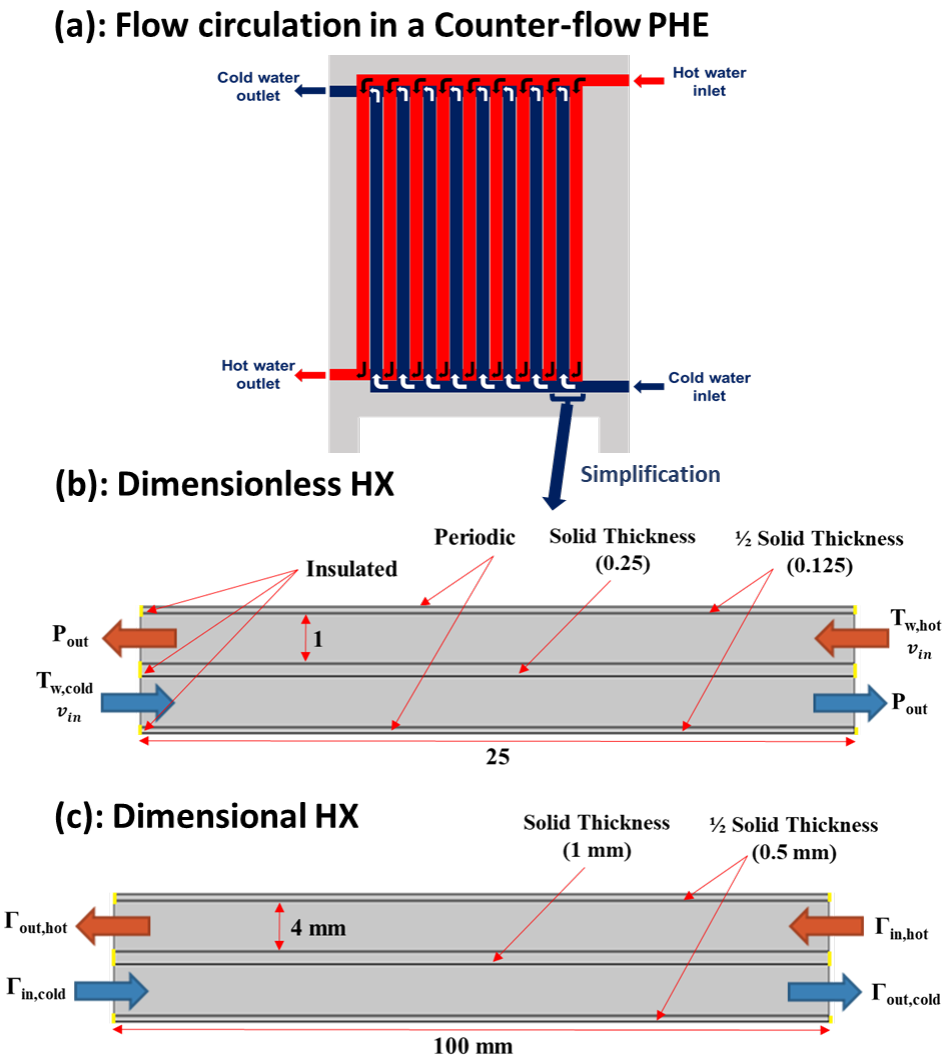

Figure 1: (a): Flow circulation in counter-flow PHE, simplified **(b)**: dimensionless, **(c)**: dimensional HX

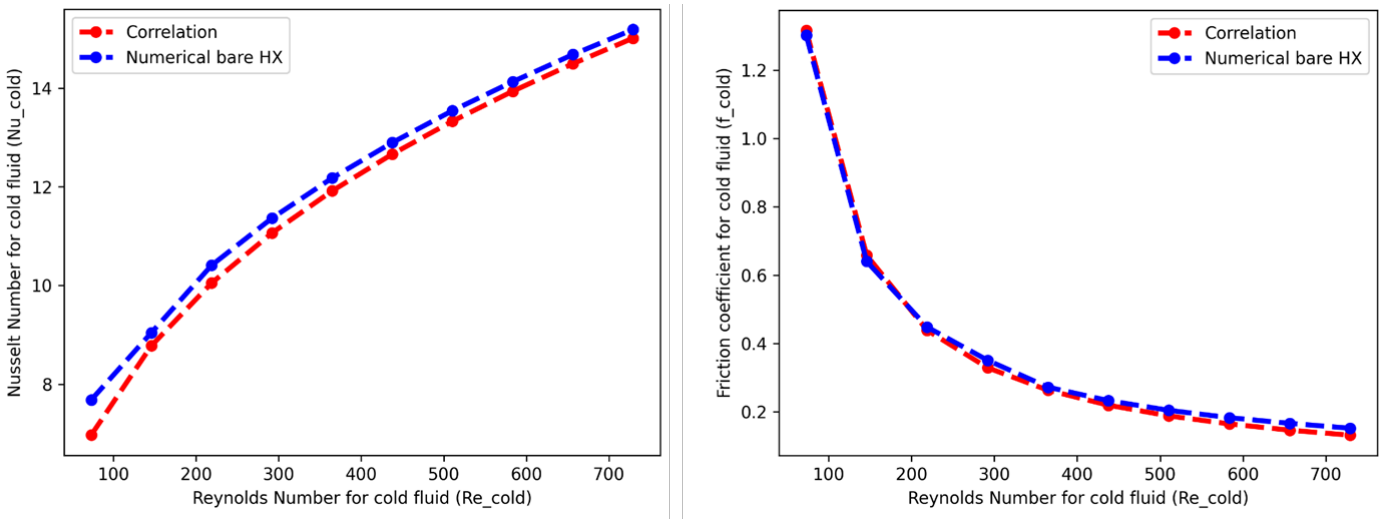

(a) : Nusselt Number (Nu) Vs Reynolds number (Re)

(b) : Friction coefficient (f) Vs Reynolds number (Re)

Figure 2: Comparison of the numerical results of the bare HX with theoretical correlations

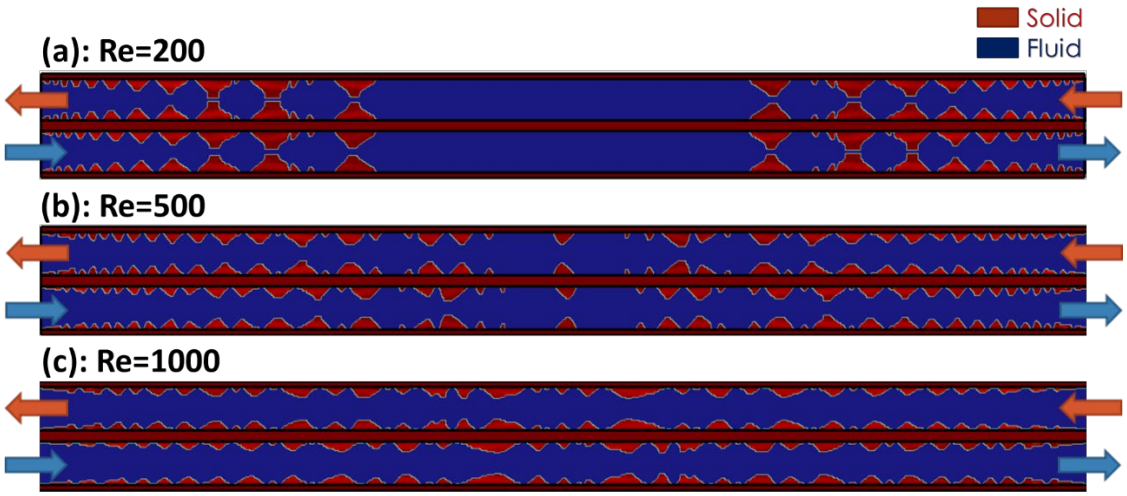

Figure 3: Acquired topologies at **(a)** Re=200,**(b)** Re=500,**(c)** Re=1000 with Pr_f=6.85 & C_k=10.

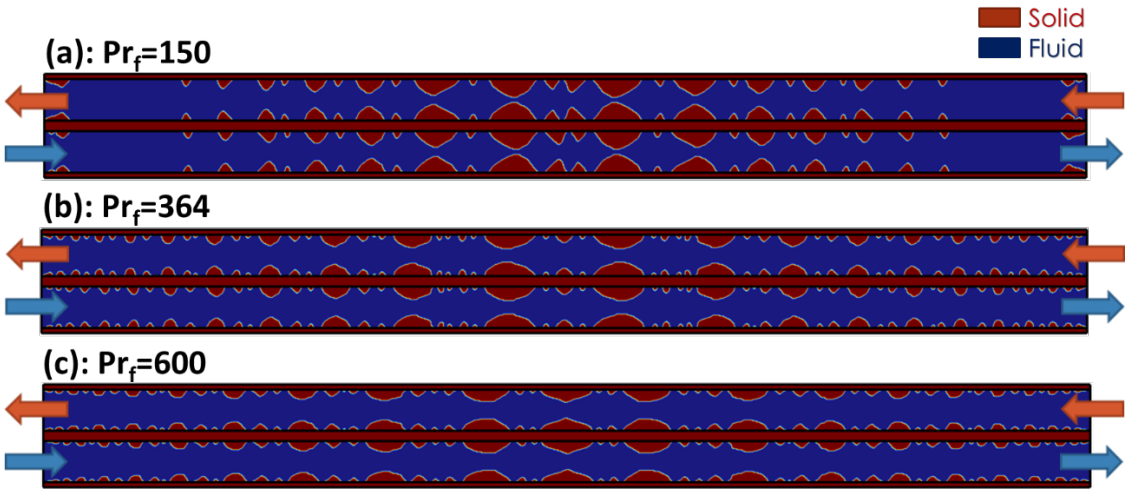

Figure 4: Acquired topologies at **(a)** Pr_f=150, **(b)** Pr_f=364, **(c)** Pr_f=600 with Re=100 and C_k=150.

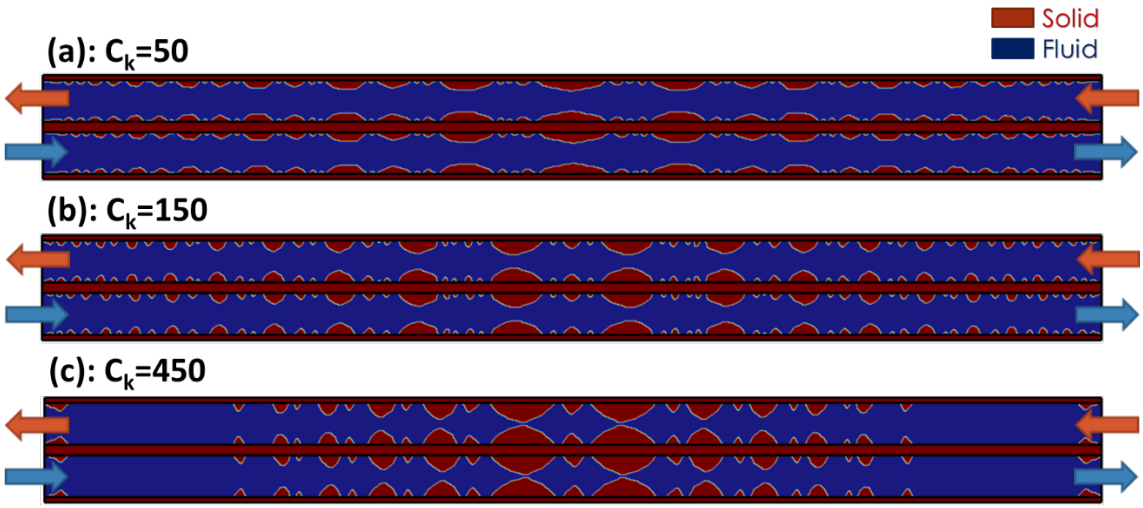

Figure 5: Generated topologies at **(a)** C_k=50, **(b)** C_k=150, **(c)** C_k=450 with Re=100 & Pr_f=364.

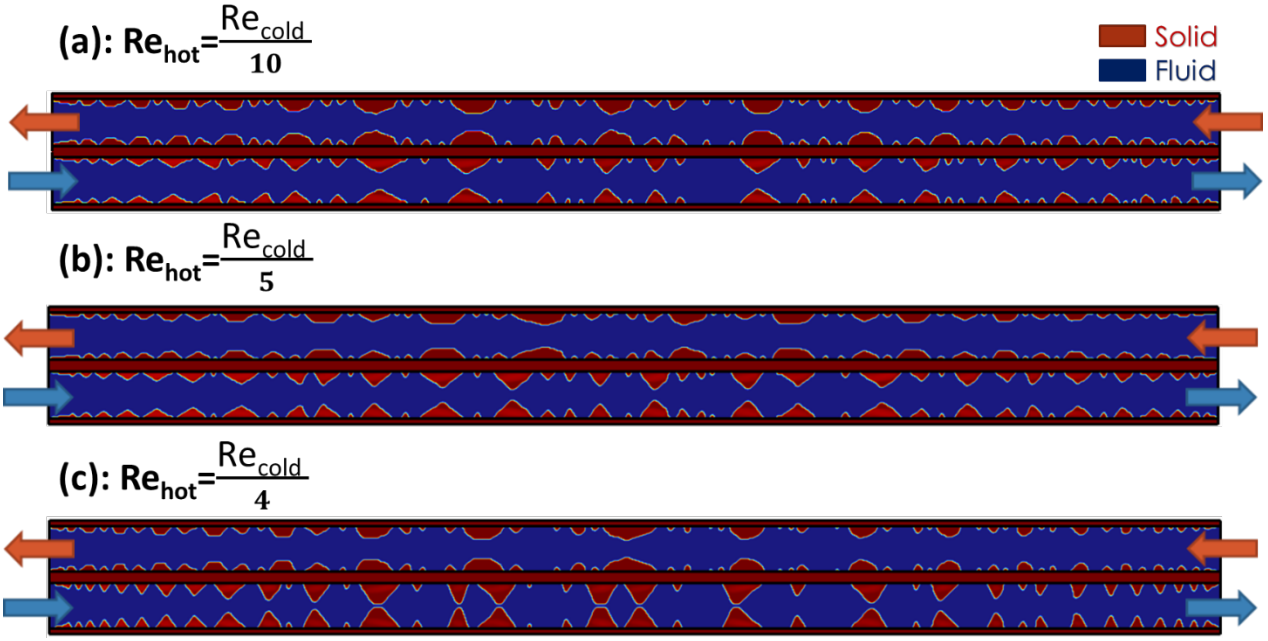

Figure 6: Effect of Reynolds number ratio (Re_{cold}/Re_{hot}) on the acquired topologies for Pr_{cold}=6.85, Pr_{hot}=364, $C_{k(cold)}$=10,$C_{k(hot)}$=61.

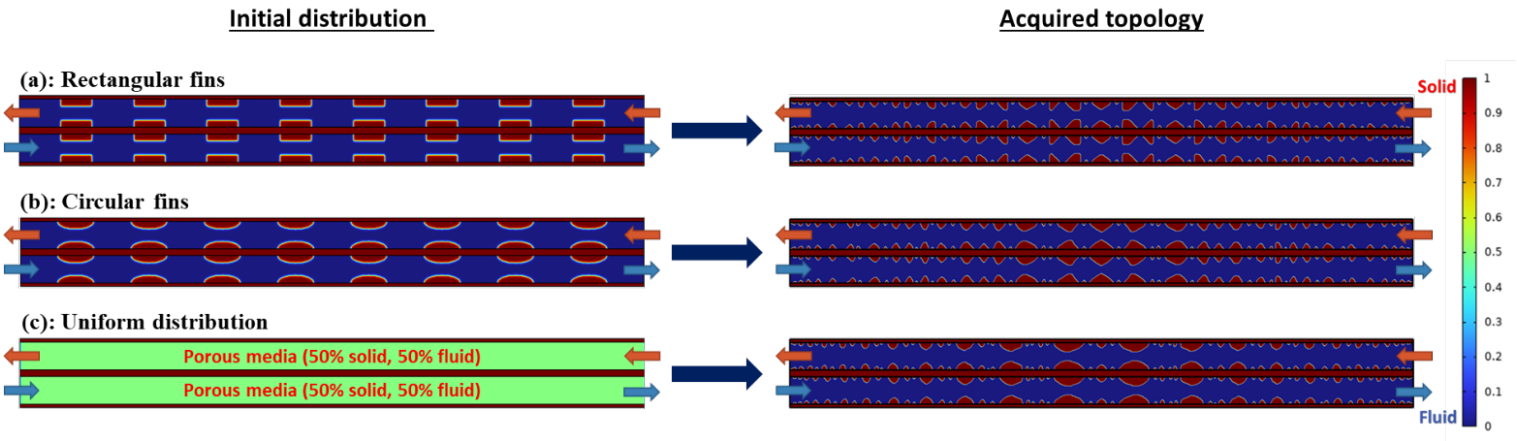

Figure 7: Generated topologies by starting with **(a)** Rectangular fins , **(b)** Circular fins, **(c)** uniform distribution as initial topology for Re=100, Pr=364,C_k =150.

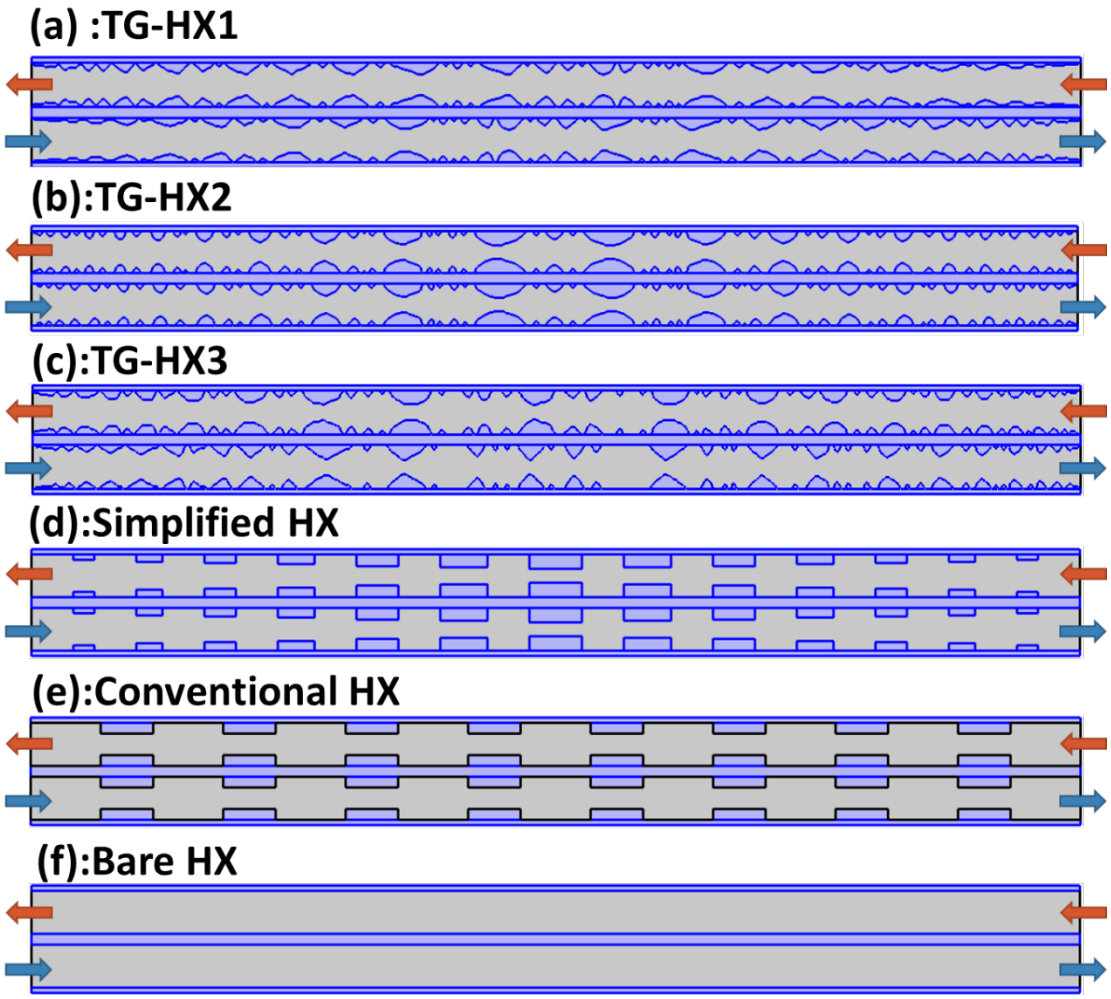

Figure 8: (a) TG-HX1, **(b)** TG-HX2, **(c)** TG-HX3, **(d)** Simplified HX, **(e)** Conventional HX and **(f)** Bare HX units.

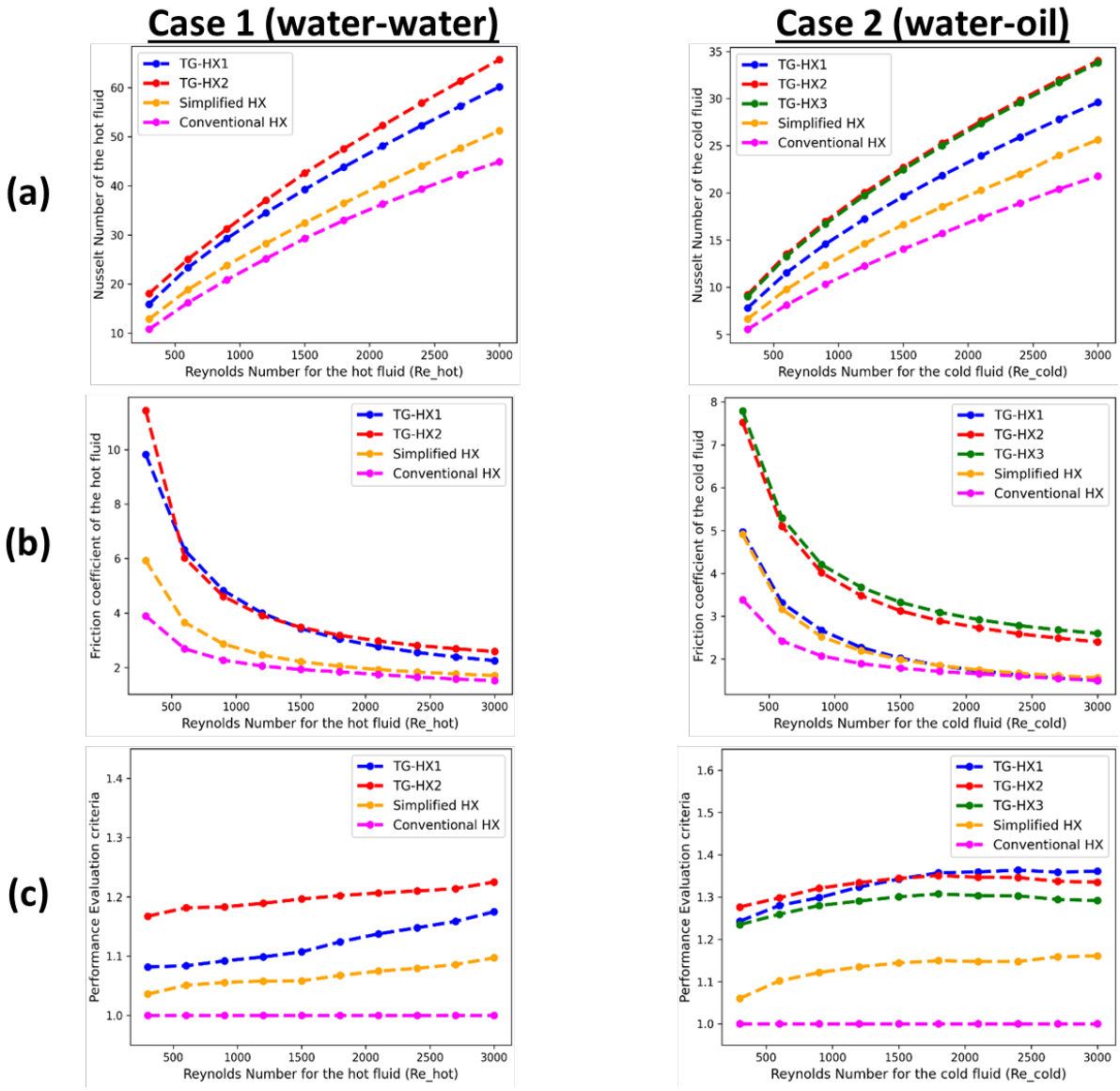

Figure 9: Variation of **(a)**: the Nusselt Number (*Nu*), **(b)**: friction coefficient (*f*) and **(c)**: Performance evaluation criteria (PEC) with respect to the Reynolds number for all HX units in cases 1 & 2.

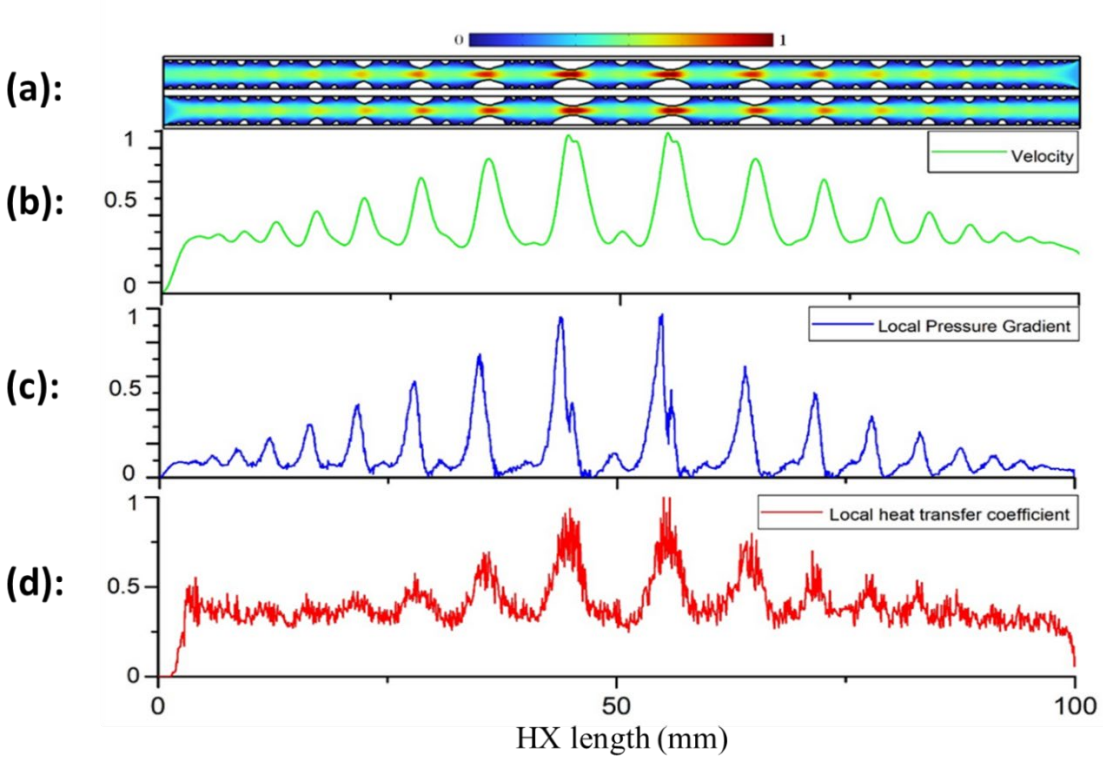

Figure 10: Normalized **(a)** velocity contours, **(b)** velocity plot, **(c)** local pressure drop, **(d)** local heat transfer coefficient based on their maximum value over the TG-HX2 at Re_{hot}=300.

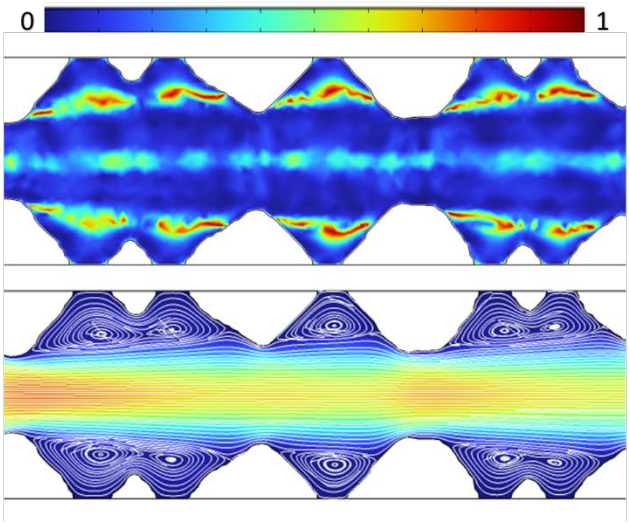

(a): Synergy field number distribution (Top), Velocity streamlines (Bottom)

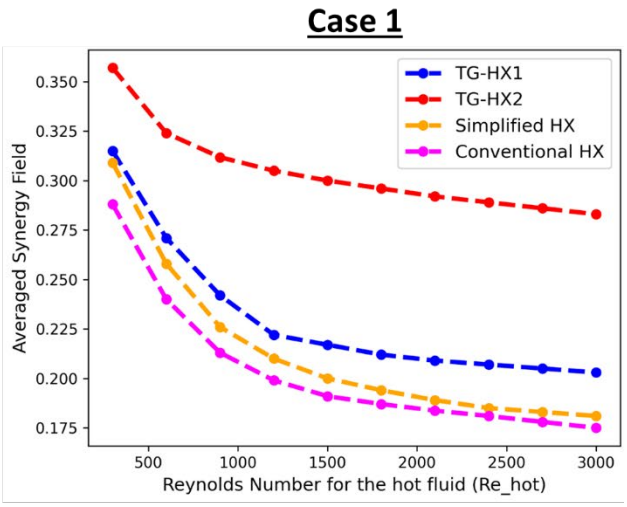

(b): Synergy field number Vs Re

Figure 11: Synergy field number variation with regards to the HX's length and Reynolds number

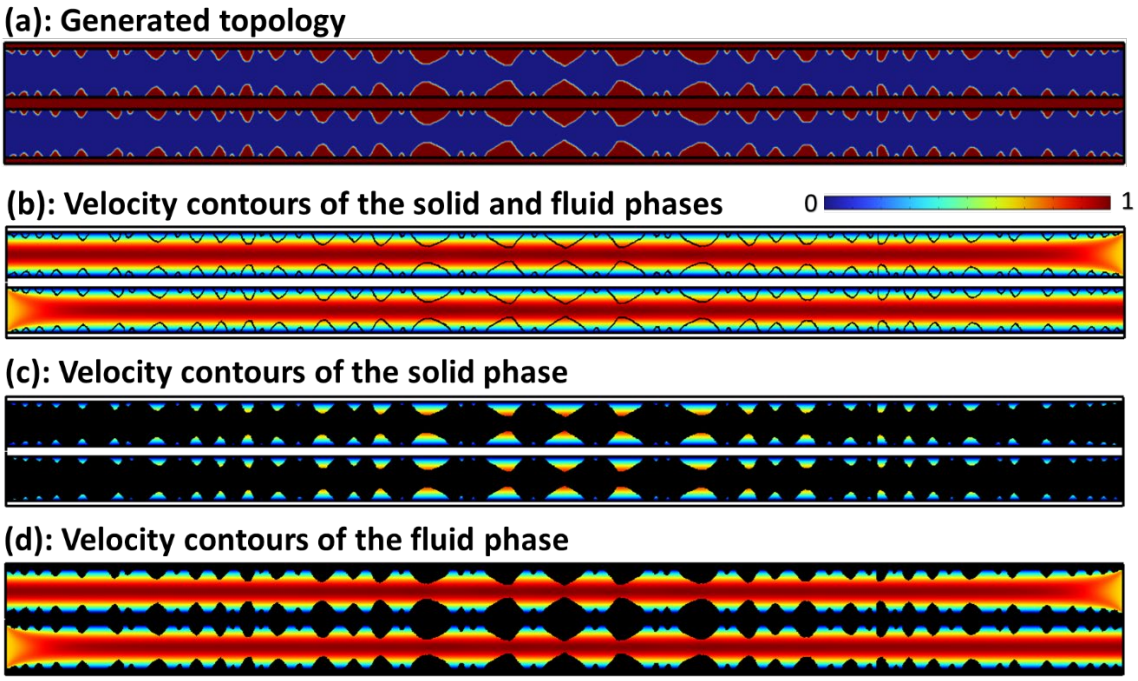

Figure 12: **(a):** Generated topology and the corresponding normalized velocity contours for **(b):** solid and fluid phases, **(c):** solid phase and **(d):** fluid phase